J Nanopart Res (2017) 19: 315
DOI 10.1007/s11051-017-4016-2

BRIEF COMMUNICATION

A comparative study on the morphology of P3HT:PCBM solar cells with the addition of Fe_3O_4 nanoparticles by spin and rod coating methods

Wenluan Zhang · Ngoc A. Nguyen · Roy Murray · Jiyuan Xin · Michael E. Mackay

Received: 10 May 2017 / Accepted: 31 August 2017 / Published online: 9 September 2017

Abstract Our previous study presented up to 20% power conversion efficiency (PCE) enhancement of poly(3-hexylthiophene):phenyl-C_{61}-butyric acid methyl ester (P3HT:PCBM) solar cells under the Fe_3O_4 nanoparticles (NPs) self-assembly (SA) effect by spin coating. Fe_3O_4 NPs (about 11 nm hydrodynamic diameter) form a thin layer at the top interface of the light absorbing active layer, which results in the generation of PCBM rich region improving the charge transport (Zhang et al. Sol Energ Mat Sol C 160:126–133, 2017). In order to investigate the feasibility of this Fe_3O_4 NPs SA effect under large-scale production condition, a smooth rod was implemented to mimic roll-to-roll coating technique and yield active layers having about the same thickness as the spin-coated ones. Small angle neutron scattering and grazing incidence X-ray diffraction were employed finding out similar morphologies of the active layers by these two coating techniques. However, rod-coated solar cell's PCE decreases with the addition of Fe_3O_4 NPs compared with the one without them. This is because PCBM rich region is not created at the top interface of the active layer due to the absence of Fe_3O_4 NPs, which is attributed to the weak convective flow and low diffusion rate. Moreover, in the rod-coated solar cells, the presence of Fe_3O_4 NPs causes decrease in P3HT crystallinity, thus the charge transport and the device performance. Our study confirms the role of spin coating in the Fe_3O_4 NPs SA effect and enables researchers to explore this finding in other polymer nanocomposite systems.

Keywords Energy conversion · Morphology · Fe_3O_4 nanoparticles self-assembly · Polymer solar cells · Spin coating · Rod coating · Convective flow · Diffusion rate

Electronic supplementary material The online version of this article (https://doi.org/10.1007/s11051-017-4016-2) contains supplementary material, which is available to authorized users.

W. Zhang (✉)
School of Automation Engineering, University of Electronic Science and Technology of China, Chengdu, 611731, China
e-mail: wenluanzh@uestc.edu.cn

W. Zhang · N. A. Nguyen · M. E. Mackay
Department of Materials Science and Engineering, University of Delaware, Newark, DE 19716, USA

M. E. Mackay
e-mail: mem@udel.edu

R. Murray
Department of Physics and Astronomy, University of Delaware, Newark, DE, 19716, USA

J. Xin · M. E. Mackay
Department of Chemical and Biomolecular Engineering, University of Delaware, Newark, DE 19716, USA

Introduction

During the past two decades, great interests have been attracted in the field of organic photovoltaics (OPV), especially for polymer solar cells, because of their potential low cost manufacturing process, flexible substrates, and environmental friendliness (Treat and Chabinyc 2014; Krebs et al. 2014; Youn et al. 2015; Li et al. 2017). The light absorbing active layer of a polymer solar cell is, commonly, a blend of semiconducting polymer (electron donor, such as poly(3-hexyl thiophene), i.e., P3HT) and fullerene derivative molecules (electron acceptor, such as [6,6]-phenyl-C_{61}-butyric acid methyl ester, i.e., PCBM). In a representative P3HT:PCBM polymer solar cell, a Coulomb-bound electron-hole pair, i.e., exciton, is created when a photon is absorbed by P3HT. The exciton then transports to the interface of P3HT and PCBM for separation to generate charge carriers. Due to the relatively short diffusion length (approximately 10 nm) of the exciton, an interpenetrating mixture of polymer and fullerene derivative molecules is proposed as so-called bulk-heterojunction (BHJ) to optimize the device performance (Dang et al. 2013). A vertical comb-like interdigitated structure of electron donor and acceptor materials is believed to be the ideal BHJ morphology for a polymer solar cell (Coakley and McGehee 2004). Hence, how to achieve such a delicate nanostructure in order to obtain high power conversion efficiency (PCE) has been extensively studied (Germack et al. 2010; Rogers et al. 2011; Hong et al. 2014; Huang et al. 2014; Heeger 2014).

Recently, we reported up to 20% PCE enhancement of P3HT:PCBM solar cells by mixing 4 vol% Fe_3O_4 nanoparticles (NPs) in the light absorbing active layers. Since Fe_3O_4 NPs do not scatter light and are insulators, so optical effect and electronic properties from these NPs can be excluded to simplify the morphological study on this system. Having the solution blend of P3HT, PCBM, and Fe_3O_4 NPs, all the materials transport to the air interface of the active layer, i.e., cathode side, by convective flow and solvent evaporation in the spin coating process. These three components form a pseudo-layered structure following their surface energy ordering. Thus, a thin layer of Fe_3O_4 NPs is formed to develop polymer depletion zone repelling P3HT away from the cathode interface. As a result, PCBM molecules fill up the spaces left by P3HT creating PCBM rich region which benefits the electron transport and collection at the cathode interface. In the utilization of this Fe_3O_4 NPs self-assembly (SA) effect, spin coating creates strong convective flow and fast solvent evaporation (Zhang et al. 2017). This coating technique is usually applied to produce small area thin films, such as bio-sensors and organic electronic devices due to its good controllability and versatility (Hou et al. 2011; van Franeker et al. 2015; Wu et al. 1601). However, considerable amount of solution is wasted in the substrate spinning step and it is not compatible with the roll-to-roll (R2R) coating, which is commonly used to fabricate flexible solar cell modules in large volume (Chou et al. 2013; Xiong et al. 2015; Andersen et al. 2011; Apilo et al. 2015).

Due to the differences between these two techniques, when R2R coating is in use to produce solar cell devices, the Fe_3O_4 NPs SA effect comes under question. Hence, the objective of this study is to investigate the feasibility of this NPs SA effect under R2R coating condition and compare the results with the spin-coated ones. In laboratories, smooth rod can be used to mimic R2R coating without the implementation of a large facility, which provides convenience to this work (Hu et al. 2010). Device performance data were presented through current-density–voltage (J–V) characterization. Morphological differences between spin- and rod-coated active layers were studied by various characterization techniques. Transmission electron microscopy (TEM) was used to observe the cross-sections of active layers and investigate the influence of the two coating methods on the distribution of Fe_3O_4 NPs.

Experimental section

Sample preparation and characterization are similar as stated in previous report (Zhang et al. 2017). A smooth rod was applied to mimic the R2R coating technique. Here, we provide a brief description as follows. Indium tin oxide (ITO)-coated one inch square glasses (resistance of 8–12 Ω/□, from Delta technologies, LTD) were treated by ultrasonic cleaner in acetone and isoproponal sequentially for 10 min. Ultraviolet ozone plasma was applied on all the substrates for 15 min. A 33-nm thick layer of poly(3,4-ethylenedioxythio-phene):poly(styrenesulfonate)

(PEDOT:PSS, from H.C. Starck, Al 4083) was spin coated on the substrate, which was then annealed for 20 min at about 130 °C. All the substrates were transferred to a nitrogen-filled glove box. In it, P3HT (from Luminescence Technology Corp., $M_n = 55,000$ g/mol, polymer dispersity index (PDI) = 1.4) and PCBM (from Nano-C) were dissolved in di-*ortho*-chlorobenzene with 1:1 weight ratio in a total 40 mg/ml concentration. 4 vol% of Fe_3O_4 NPs (EMG1300, hydrodynamic diameter 11 nm, density 2.85 g/cm^3, from Ferrotec), with respect to the P3HT:PCBM solid content, was mixed into the P3HT:PCBM solution. The solution was stirred 24 h at 40 °C in order to have complete dissolution. Then, it was filtered through a 0.45-μm Teflon filter before the coating step. For spin-coated active layers, 600 rpm and 60 s were used to obtain approximately 230 nm thickness. To achieve about the same thickness from rod coating, the substrate was placed on a polytetrafluoroethylene (PTFE) plate and fixed between two glass slides. A drop of solution was deposited on it, then the smooth rod swept back and forth five times to make the film (see Fig. S1). All the samples were thermal annealed at 110 °C for 10 min yielding high degree of P3HT polycrystalline. LiF (0.8 nm) and Al (80 nm) were sequentially thermal evaporated on the active layers obtaining about 0.1 cm^2 device area. J–V tests were performed using a Keithley 2400 source meter, under illumination of 100 mW/cm^2 from 150 W solar simulator with AM1.5G filters. Eight data were collected for each sample from eight different devices under the same condition. 95% confidence interval was used to average the collected data and yield the uncertainty value. All materials were used as received.

Soda-lime glasses were used instead of ITO-coated ones for characterizations other than J–V tests. For SANS measurements, the active layer was floated off on the surface of deionized water and picked up by a 1-in. diameter (*100*) double side polished silicon wafer. Repeat five times for each wafer to have a stack of 3 wafers, i.e., 15 active layers under the same condition. By doing this, the scattering signal from the active layers can be increased significantly without considering the background noise from silicon, since (*100*) silicon wafer is virtually transparent to neutrons. The NG3 instrument in National Institute of Standards and Technology (NIST) center for neutron research was employed in this work. Two detector distances and two neutron wavelengths were used, including 4 m with a wavelength of 6 Å and 13.2 m with 8.4 Å. Rigaku Ultimate IV multipurpose XRD system was implemented to perform grazing incidence X-ray diffraction (GIXRD) measurements, incident angle of 0.5° was used. X-ray photoelectron spectroscopy (XPS) measurements were performed on a Surface Science machine using monochromated Al k-alpha radiation (1486.6 eV).

In order to obtain TEM cross-section images of an active layer, the film was floated off on the surface of deionized water and then picked up by a piece of dried epoxy resin (Spurr's kit from Electron Microscopy Sciences). After it was completely dried, a 20-nm layer of gold was sputtered on the surface

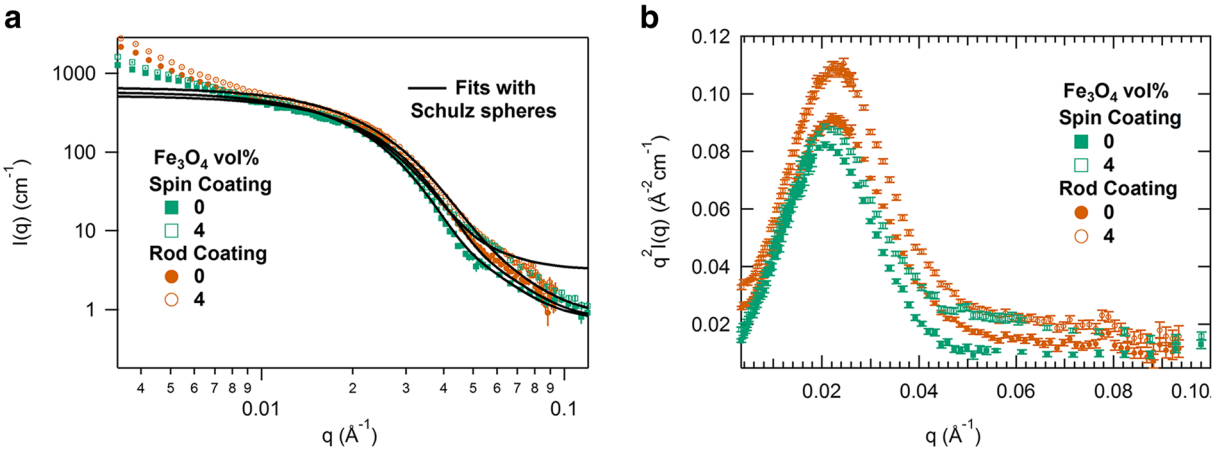

Fig. 1 **a** Absolute scattering intensity $I(q)$ as a function of wave vector q fitted by polydispersed sphere model following Schulz distribution (Schulz spheres model). **b** Kratky plots of $q^2I(q)vs.q$. for spin- and rod-coated samples

of the film as a marker layer in TEM images. Then, a drop of fresh epoxy resin was deposited on it following a 24-h curing treatment at 40 °C. Reichert Jung Microtome was applied for ultramicrotomy to obtain a film about 70–80 nm thickness ready for the TEM imaging. Transmission electron microscope JEM-2010F operated at 200 kV was used to obtain all the images.

Results and discussion

Small angle neutron scattering (SANS) curves from spin- and rod-coated active layers are presented in Fig. 1a to show the morphological properties of spin- and rod-coated active layers in detail. The absolute intensity $I(q)$ as a function of wave vector q is plotted in log-log scale. The scattering patterns from all the samples exhibit overlapped curves which indicates similar structures formed at the length scale of 1 to 7.9 nm ($2\pi/q, q$ is in the range of 0.08 to 0.6 $Å^{-1}$) caused by PCBM agglomerates (Kiel et al. 2010). This is confirmed by the Kratky plots presented as $q^2 I(q) vs. q$ in Fig. 1b. The peak displayed in low-q regime is an indicative of particle-like feature (Mackay et al. 2003; Tuteja et al. 2005). The peak position is affected by the particle size alone and the maxima of the peak is influenced by both the volume fraction of particles and neutron scattering length density (nSLD) contrast between the particles and surrounding matrix. Since all the peaks centered at almost the same position of 0.022 $Å^{-1}$ (length scale of 28.5 nm), one can tell that the rod coating method does not affect the PCBM agglomerate size. However, for rod-coated samples, longer liquid film drying time, compared with the spin-coated ones (see Fig. 2), allows more PCBM molecules agglomerate before they reach equilibrium status resulting in higher peak maxima. The addition of 4 vol% Fe_3O_4 NPs does not have significant impact on the scattering pattern, which is consistent with our previous report (Zhang et al. 2017). A quantitative analysis

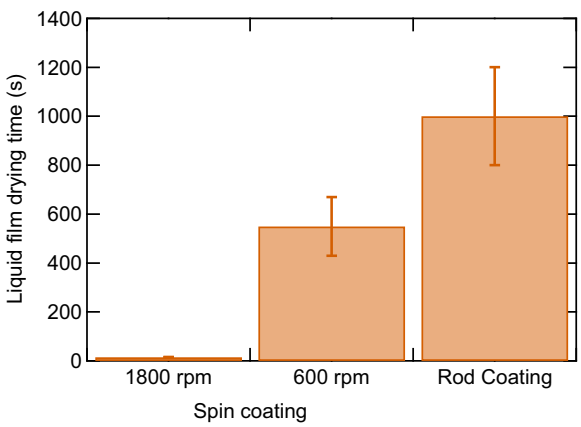

Fig. 2 Liquid film drying time under various coating conditions. Each data is collected from six samples under the same condition. The uncertainty value was calculated from 95% confidence interval setting. The drying time of rod-coated samples is about 1000 s, and the 600 rpm spin-coated ones is much lower, about 580 s, while 1800 rpm spin coating only yielded a 15-s drying time

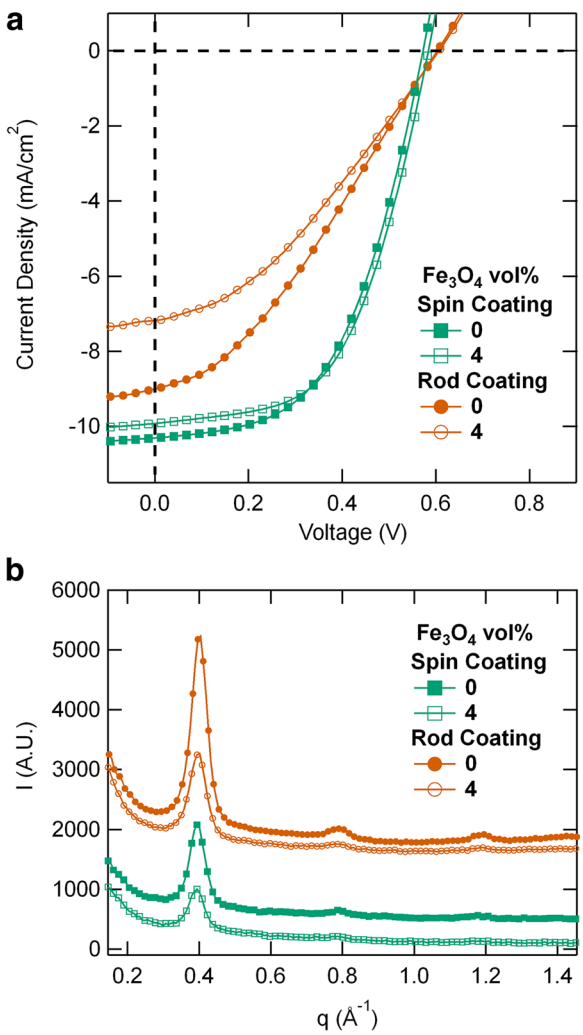

Fig. 3 **a** J–V characteristic for samples from spin and rod coating. **b** GIXRD patterns of spin- and rod-coated samples

can be made by numerical model fitting on these scattering patterns. PCBM agglomerates were treated as polydispersed hard sphere following Schulz size distribution surrounded by a matrix of P3HT and solubilized PCBM (Kotlarchyk and Chen 1983; Kline 2006; Chen et al. 2014; Zhang et al. 2016). The fitting results agree well with the qualitative analysis above. PCBM agglomerates have a radius about 7 nm, which is not affected by either the addition of Fe_3O_4 NPs or the coating methods. A bit more PCBM agglomerates are obtained from rod-coated samples. The model description and detailed fitting results are presented in supporting information.

J–V curves for samples from the spin and rod coating methods are presented in Fig. 3a. The device performance of the rod-coated samples is generally lower than the spin-coated ones because of the scratches on active layers generated during the coating process (shown in Fig. S3 and Table S1). In previous study, the addition of 4 vol% Fe_3O_4 NPs improve PCE of 90-nm thick active layer samples by 20%, while did little to 230-nm thick ones (Zhang et al. 2017). However, in this work, the addition of 4 vol% Fe_3O_4 NPs decreased the rod-coated sample's current density (J) from 8.4 to 6.7 mA/cm^2 causing the PCE lowered to 1.4 from 1.9%, which is contrary to our previous findings. To unravel its reason, P3HT polycrystalline property was first studied by GIXRD.

The GIXRD patterns presented in Fig. 3b show (*100*) peaks at 0.38 Å^{-1} rendering a d-spacing of 16.5 Å ($2\pi/q$). The height and full half width maximum (FWHM) of the peak enable one's ability to compare P3HT crystallinity qualitatively among samples (Kiel et al. 2010; Chen et al. 2011; Rivnay et al. 2012). So, one can tell that the rod-coated samples have higher degree of P3HT crystallinity because of their relatively higher peak maxima compared with the spin-coated ones. In the spin coating process, 90% solvent on the substrate is lost in the first 5 s and the amount of residual solvent is not much, if any (Chou et al. 2013). While in the rod coating process, the large amount of residual solvent left on the substrate results in much longer liquid drying time, as shown in Fig. 2. Thus, much denser solvent vapor is generated around the substrate, equivalent to solvent annealing, creating higher degree of P3HT crystallinity compared with the spin-coated ones (Li et al. 2007). However, this high degree of P3HT crystallinity did not lead to

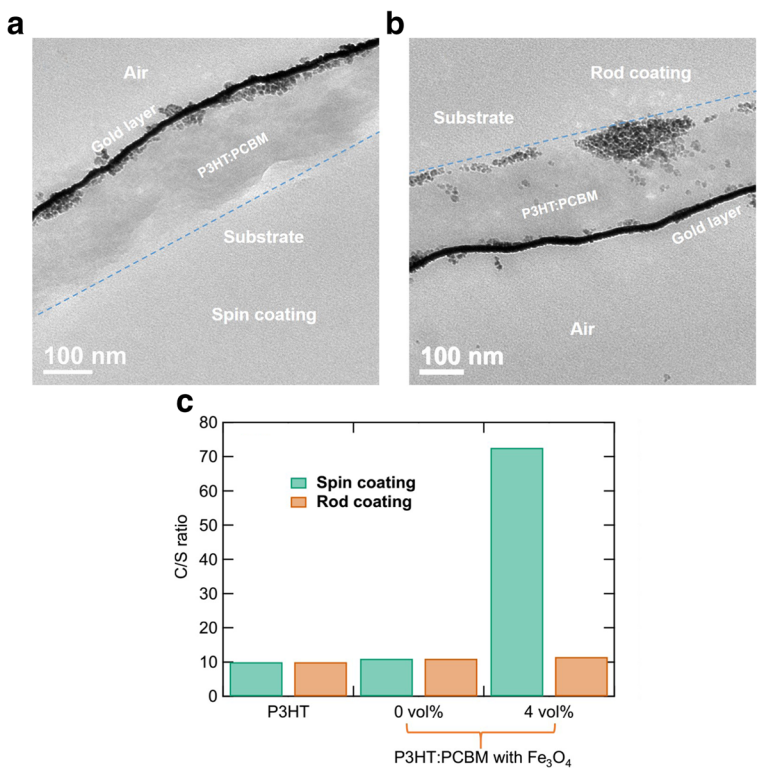

Fig. 4 Cross-section TEM images of **a** the spin- and **b** the rod-coated samples containing 4 vol% Fe_3O_4 NPs in the active layers. **c** C/S atomic ratios of the top surfaces from pure P3HT, spin- and rod-coated active layers

any device performance improvement suggesting that the PCE was dominated by the defects of active layers brought by the scratches in the rod coating process (see Fig. S3). The addition of Fe_3O_4 NPs disrupts the formation of P3HT polycrystalline further lowering the current density as shown in J–V curves.

TEM cross-section images shown in Fig. 4a and b present the vertical distribution of Fe_3O_4 NPs within the active layers. Fe_3O_4 NPs in the spin-coated sample form a thin layer at the air interface. While in the rod-coated sample, these NPs are randomly distributed and large clusters are generated at the substrate interface. As reported in the previous study, the magnetic and depletion attraction cause clustering of NPs, and Fe_3O_4 NP's density (2.85 g/cm^3) is much higher than the blend of P3HT:PCBM (about 1.2 g/cm^3), so it is possible that the Fe_3O_4 NP clusters aggregate at the substrate due to their gravitational impact. Since the coating method is the only difference during the sample preparation step, it suggests that the convective flow from spin coating is the key factor to move NPs upward to the air interface which cannot be provided by rod coating method.

In the rod-coated active layers, to achieve the same NP SA effect without strong convective flow, Fe_3O_4 NPs have to rapidly diffuse toward the air interface and form layered structure following the surface energy ordering of the film's components as they do in the spin-coated ones (Zhang et al. 2017). If we set x is the distance of particle's vertical diffusion and t is diffusion time, then we have $x = (2Dt)^{1/2}$ (Deegan et al. 1997; Rabani et al. 2003; Bigioni et al. 2006). D is diffusion coefficient and estimated from the Stokes–Einstein relation $D = k_BT/6\pi\eta$, where k_B is Boltzmann's constant, T is absolute temperature, η is dynamic viscosity, r radius of the particle. Since $\eta = 3.38$ cp for the P3HT:PCBM solution (value presented in Table S4), $k_BT = 4.11 \times 10^{-21}$J at room temperature ($T = 298$K), and Fe_3O_4 NP radius $r = 5.5$ nm, so $D = 11.7\ \mu m^2 s^{-1}$. Thus, for 1000-s liquid drying time (see Fig. 2), x is about 0.153 mm, which is much shorter than the height of solution left on the substrate (around 1 mm). Therefore, the liquid film drying rate is much faster than the NP diffusion rate. The Fe_3O_4 NPs are immobilized in the matrix of P3HT:PCBM in random distribution when the liquid film interface is descending. Hence, the polymer depletion zone cannot be generated due to the absence of a thin layer of Fe_3O_4 NPs at the air interface. As a result, the PCBM rich region cannot be obtained to improve charge transport and collection at cathode. This result was confirmed by the C/S atomic ratio shown in Fig. 4c. Since sulfur atoms are only from thiophene S of P3HT, and almost all the carbon atoms are from blend of P3HT and PCBM, so one can compare the C/S atomic ratio to know the change of PCBM composition at the top surfaces of the pure P3HT, spin- and rod-coated active layers (Zhang et al. 2017). For the rod-coated sample, with the addition of Fe_3O_4 NPs, its composition is almost the same as pure P3HT meaning very little PCBM found at the air interface, which agrees well with the TEM images and justifies our argument.

Previously, a group of researchers claimed that the spin-orbit coupling effect caused the device performance improvement with the addition of Fe_3O_4 NPs (González et al. 2015). This proposed mechanism argued that the improvement relied on the proper concentration of Fe_3O_4 NPs doped in the active layer without taking account of the NPs' vertical distribution in the active layer. Based on this proposed mechanism, device performance improvement should be obtained in the rod-coated samples with the addition of 4 vol% Fe_3O_4 NPs, which is contrary to our findings in this study, which put this spin-orbit coupling effect under question requiring further proof for justification.

Conclusion

Although the rod coating technique is simple and fast for large-scale fabrication of organic solar cell devices, the morphology control method effective for spin-coated solar cells may not function properly for rod coating process. Without strong convective flow and solvent evaporation from the rapid initial drying of the liquid film, Fe_3O_4 NPs cannot diffuse to the cathode interface because of the viscous resisting force and low solvent evaporation rate resulting in a low NP diffusion rate. In order to obtain high NP diffusion rate, a solvent with low viscosity or boiling point could be considered as a replacement of di-chlorobenzene. Heating the liquid films could also be an option since it can increase the solvent evaporation rate thus NP diffusion. However, the liquid

film drying rate is also increased, which complicates the morphology control process. After all, this study shows that the P3HT:PCBM morphology at nanometer length scale remains more or less unchanged by using the rod coating technique and there is potential for scalable manufacturing if we could transfer the morphology control methods in the laboratory to the industrial level. It also paves the way for further research on the NP SA effect leading to clever design and functionalization concepts in electronic devices made of nanocomposite materials.

Acknowledgements This paper's writing was supported by the UESTC's New Faculty Fund. Experimental work of this study was accomplished at University of Delaware during Dr. Zhang's PhD studies. It was supported by NIST Award 70NANB10H256 through the Center for Neutron Science at University of Delaware. The authors acknowledge the support from National Institute of Standards and Technology, U.S. Department of Commerce, in providing the neutron research facilities used in this work. The authors also thank Prof. David Martin for usage of the UV-vis spectrometer. Mr. Frank Kriss and Prof. Chaoying Ni's help on the use of microtome is greatly appreciated.

Compliance with Ethical Standards

Conflict of interest The authors declare that they have no conflict of interest.

References

Andersen TR, Larsen-Olsen TT, Andreasen B, Boittiger APL, Carle JE, Helgesen M, Bundgaard E, Norrman K, Andreasen JW, Jorgensen M, Krebs FC (2011) Aqueous processing of low-band-gap polymer solar cells using roll-to-roll methods. ACS Nano 5(5):4188–4196. https://doi.org/10.1021/nn200933r

Apilo P, Hiltunen J, Valimaki M, Heinilehto S, Sliz R, Hast J (2015) Roll-to-roll gravure printing of organic photovoltaic modules–insulation of processing defects by an interfacial layer. Prog Photovolt 23(7):918–928. https://doi.org/10.1002/pip.2508

Bigioni TP, Lin XM, Nguyen TT, Corwin EI, Witten TA, Jaeger HM (2006) Kinetically driven self assembly of highly ordered nanoparticle monolayers. Nat Mater 5(4):265–270. https://doi.org/10.1038/nmat1611

Chen D, Nakahara A, Wei D, Nordlund D, Russell TP (2011) P3HT/PCBM bulk heterojunction organic photovoltaics: correlating efficiency and morphology. Nano Lett 11(2):561–567. https://doi.org/10.1021/nl103482n

Chen HP, Hsiao YC, Hu B, Dadmun M (2014) Tuning the morphology and performance of low bandgap polymer: fullerene heterojunctions via solvent annealing in selective solvents. Adv Funct Mater 24(32):5129–5136. https://doi.org/10.1002/adfm.201400552

Chou KW, Yan B, Li R, Li EQ, Zhao K, Anjum DH, Alvarez S, Gassaway R, Biocca A, Thoroddsen ST, Hexemer A, Amassian A (2013) Spin-cast bulk heterojunction solar cells: a dynamical investigation. Adv Mater 25(13):1923–1929. https://doi.org/10.1002/adma.201203440

Coakley KM, McGehee MD (2004) Conjugated polymer photovoltaic cells. Chem Mater 16(23):4533–4542. https://doi.org/10.1021/cm049654n

Dang MT, Hirsch L, Wantz G, Wuest JD (2013) Controlling the morphology and performance of bulk heterojunctions in solar cells. Lessons learned from the benchmark poly(3-hexylthiophene):[6,6]-phenyl-C_{61}-butyric acid methyl ester system. Chem Rev 113(5):3734–3765. https://doi.org/10.1021/cr300005u

Deegan RD, Bakajin O, Dupont TF, Huber G, Nagel SR, Witten TA (1997) Capillary flow as the cause of ring stains from dried liquid drops. Nature 389(6653):827–829. https://doi.org/10.1038/39827

Germack DS, Chan CK, Kline RJ, Fischer DA, Gundlach DJ, Toney MF, Richter LJ, DeLongchamp DM (2010) Interfacial segregation in polymer/fullerene blend films for photovoltaic devices. Macromolecules 43(8):3828–3836. https://doi.org/10.1021/ma100027b

González DM, Körstgens V, Yao Y, Song L, Santoro G, Roth SV, Müller-Buschbaum P (2015) Improved power conversion efficiency of P3HT:PCBM organic solar cells by strong spin–orbit coupling-induced delayed fluorescence. Adv Energy Mater 5(8):1401, 770. https://doi.org/10.1002/aenm.201401770

Heeger AJ (2014) 25th anniversary article: bulk heterojunction solar cells: understanding the mechanism of operation. Adv Mater 26(1):10–28. https://doi.org/10.1002/adma.201304373

Hong S, Yi M, Kang H, Kong J, Lee W, Kim JR, Lee K (2014) Effect of solvent on large-area polymer-fullerene solar cells fabricated by a slot-die coating method. Sol Energ Mat Sol C 126:107–112. https://doi.org/10.1016/j.solmat.2014.03.042

Hou L, Wang E, Bergqvist J, Andersson BV, Wang Z, Müller C, Campoy-Quiles M, Andersson MR, Zhang F, Inganäs O (2011) Lateral phase separation gradients in spin-coated thin films of high-performance polymer:fullerene photovoltaic blends. Adv Funct Mater 21(16):3169–3175. https://doi.org/10.1002/adfm.201100566

Hu L, Kim HS, Lee JY, Peumans P, Cui Y (2010) Scalable coating and properties of transparent, flexible, silver nanowire electrodes. ACS Nano 4(5):2955–2963. https://doi.org/10.1021/nn1005232

Huang Y, Kramer EJ, Heeger AJ, Bazan GC (2014) Bulk heterojunction solar cells: morphology and performance relationships. Chem Rev 114(14):7006–7043. https://doi.org/10.1021/cr400353v

Kiel JW, Eberle APR, Mackay ME (2010) Nanoparticle agglomeration in polymer-based solar cells. Phys Rev Lett 168(16):701. https://doi.org/10.1103/PhysRevLett.105.168701

Kline S (2006) Reduction and analysis of SANS and USANS data using IGOR Pro. J Appl Crystallogr 39(6):895–900. https://doi.org/10.1107/S0021889806035059

Kotlarchyk M, Chen SH (1983) Analysis of small angle neutron scattering spectra from polydisperse interacting colloids. J Chem Phys 79(5):2461–2469. https://doi.org/10.1063/1.446055

Krebs FC, Espinosa N, Hosel M, Sondergaard RR, Jorgensen M (2014) A 25th anniversary article: rise to power–OPV-based solar parks. Adv Mater 26(1):29–39. https://doi.org/10.1002/adma.201302031

Li G, Yao Y, Yang H, Shrotriya V, Yang G, Yang Y (2007) Solvent annealing effect in polymer solar cells based on poly(3-hexylthiophene) and methanofullerenes. Adv Funct Mater 17(10):1636–1644. https://doi.org/10.1002/adfm.200600624

Li M, Gao K, Wan X, Zhang Q, Kan B, Xia R, Liu F, Yang X, Feng H, Ni W, Wang Y, Peng J, Zhang H, Liang Z, Yip HL, Peng X, Cao Y, Chen Y (2017) Solution-processed organic tandem solar cells with power conversion efficiencies >12%. Nat Photon 11(2):85–90. https://doi.org/10.1038/nphoton.2016.240

Mackay ME, Dao TT, Tuteja A, Ho DL, Van Horn B, Kim HC, Hawker CJ (2003) Nanoscale effects leading to non-Einstein-like decrease in viscosity. Nat Mater 2(11):762–766. https://doi.org/10.1038/nmat999

Rabani E, Reichman DR, Geissler PL, Brus LE (2003) Drying-mediated self-assembly of nanoparticles. Nature 426(6964):271–274. https://doi.org/10.1038/nature02087

Rivnay J, Mannsfeld SC, Miller CE, Salleo A, Toney MF (2012) Quantitative determination of organic semiconductor microstructure from the molecular to device scale. Chem Rev 112(10):5488–519. https://doi.org/10.1021/cr3001109

Rogers JT, Schmidt K, Toney MF, Kramer EJ, Bazan GC (2011) Structural order in bulk heterojunction films prepared with solvent additives. Adv Mater 23(20):2284–2288. https://doi.org/10.1002/adma.201003690

Treat ND, Chabinyc ML (2014) Phase separation in bulk heterojunctions of semiconducting polymers and fullerenes for photovoltaics. Annu Rev Phys Chem 65(1):59–81. https://doi.org/10.1146/annurev-physchem-040513-103712

Tuteja A, Mackay ME, Hawker CJ, Van Horn B (2005) Effect of ideal, organic nanoparticles on the flow properties of linear polymers: non-Einstein-like behavior. Macromolecules 38(19):8000–8011. https://doi.org/10.1021/ma050974h

van Franeker JJ, Westhoff D, Turbiez M, Wienk MM, Schmidt V, Janssen RAJ (2015) Controlling the dominant length scale of liquid-liquid phase separation in spin-coated organic semiconductor films. Adv Funct Mater 25(6):855–863. https://doi.org/10.1002/adfm.201403392

Wu WR, Su CJ, Chuang WT, Huang YC, Yang PW, Lin PC, Chen CY, Yang TY, Su AC, Wei KH, Liu CM, Jeng US (1601) Surface layering and supersaturation for top-down nanostructural development during spin coating of polymer/fullerene thin films. Adv Energy Mater 6(22):842. https://doi.org/10.1002/aenm.201601842

Xiong K, Hou L, Wu M, Huo Y, Mo W, Yuan Y, Sun S, Xu W, Wang E (2015) From spin coating to doctor blading: a systematic study on the photovoltaic performance of an isoindigo-based polymer. Sol Energ Mat Sol C 132:252–259. https://doi.org/10.1016/j.solmat.2014.08.039

Youn H, Park HJ, Guo LJ (2015) Organic photovoltaic cells: from performance improvement to manufacturing processes. Small 11(19):2228–2246. https://doi.org/10.1002/smll.201402883

Zhang W, Shen H, Guralnick BW, Kirby BJ, Nguyen NA, Remy R, Majkrzak CF, Mackay ME (2016) Correlation between morphology and device performance of pbttt:pc71bm solar cells. Sol Energ Mat Sol C 155:387–396. https://doi.org/10.1016/j.solmat.2016.06.042

Zhang W, Nguyen NA, Murray R, Mackay ME (2017) Device performance enhancement of polymer solar cells by nanoparticle self-assembly. Sol Energ Mat Sol C 160:126–133. https://doi.org/10.1016/j.solmat.2016.10.030